Journal of Photochemistry and Photobiology A: Chemistry 198 (2008) 221–231

Contents lists available at ScienceDirect

Journal of Photochemistry and Photobiology A: Chemistry

journal homepage: www.elsevier.com/locate/jphotochem

The photophysics of flavins: What makes the difference between gas phase and aqueous solution?

Susanne Salzmann[a], Jörg Tatchen[a,b], Christel M. Marian[a,*]

[a] Institute of Theoretical and Computational Chemistry, Heinrich Heine University Düsseldorf, Universitätsstr. 1, D-40225 Düsseldorf, Germany
[b] Chemical Physics Department, Weizmann Institute of Science, 76100 Rehovot, Israel

ARTICLE INFO

Article history:
Received 2 January 2008
Received in revised form 4 March 2008
Accepted 21 March 2008
Available online 1 April 2008

Keywords:
Flavins
Multi-reference configuration interaction
Excited states
Solvatochromism
Intersystem crossing rate constants

ABSTRACT

The ground and low-lying excited electronic states of isoalloxazine, 10-methylisoallox-azine and lumiflavin, three flavin-related compounds, were investigated by means of quantum chemical methods. Minimum structures were determined employing (time-dependent) Kohn–Sham density functional theory. Spectral properties were computed utilizing a combined density functional and multi-reference configuration interaction (DFT/MRCI) method. Solvent effects were mimicked by a conductor like screening model and micro-hydration with four explicit water molecules. At selected points along a linearly interpolated path connecting the Franck–Condon region and the S_1 minimum, spin–orbit interaction was computed employing a nonempirical mean-field Hamiltonian. For isoalloxazine, intersystem crossing (ISC) rate constants were computed, taking both direct and vibronic spin–orbit coupling into account.

On the basis of these calculations we suggest the following photo relaxation model. In the vacuum, efficient ISC ($k_{ISC} \approx 10^9\ s^{-1}$) takes place between the primarily excited $^1(\pi \rightarrow \pi^*)$ state (S_1) and the lowest $^3(n \rightarrow \pi^*)$ state (T_2). The energetic proximity of the $^1(n \rightarrow \pi^*)$ state (S_2) enhances the nonradiative relaxation of S_1 by internal conversion (IC). In aqueous solution these ISC and IC channels are energetically not accessible due to the blue shift of the $(n \rightarrow \pi^*)$ states. The high triplet quantum yield observed in experiment [J.T.M. Kennis, S. Crosson, M. Gauden, I.H.M. van Stokkum, K. Moffat, R. van Grondelle, Biochemistry 42 (2003) 3385–3392] is explained by the intersection between the $^1(\pi \rightarrow \pi^*)$ state (S_1) potential energy hypersurface (PEH) and the second $^3(\pi \rightarrow \pi^*)$ (T_2) PEH along the relaxation pathway and the strong enhancement of their spin–orbit coupling by vibronic interactions. The calculated ISC rate for this channel ($k_{ISC} \approx 10^8\ s^{-1}$) is in good agreement with experimental results. According to our model, lack of an efficient IC channel leads to an increased fluorescence quantum yield in aqueous solution.

1. Introduction

In recent years flavins have received growing attention especially due to their decisive role in blue light-mediated signal transduction in plants and bacteria [1–3]. They serve, for example, as cofactors in phototropins (phot), plasma membrane-associated proteins which are primary photoreceptors for the mediation of phototropic plant movement. Two light, oxygen and voltage-sensitive (LOV) domains are present in each phot protein which both bind one flavin mononucleotide (FMN) noncovalently. Upon absorption of blue light, the LOV domain undergoes a photocycle that leads to photobleaching. The primary step after light absorption hereby involves a rapid decay of the excited singlet state to the lowest excited triplet state via an intersystem crossing (ISC) mechanism. In a second step a metastable covalent adduct of a nearby cysteine residue and the isoalloxazine framework of the chromophor is generated resulting in a structural signal that affects autophosphorylation.

The environmental effects of the LOV domains on the photophysics of the FMN chromophore have been the topic of several experimental studies [4–8]. The experimental ISC rate constants for FMN are $k_{ISC} = 10^8\ s^{-1}$ in water (pH 7.0) and $k_{ISC} = 3 \times 10^8\ s^{-1}$ in the LOV2 domain at ambient temperatures [4]. In both cases the measured triplet quantum yield ϕ_T amounts to 0.60. In comparison to free FMN in water, the FMN in the LOV1 and LOV2 domains show a decrease of the fluorescence quantum yield Φ_F and the fluorescence lifetime τ_F by roughly a factor of two [4].

The chromophore of the LOV domain, FMN can be divided into two parts: (A) the isoalloxazine (benzol[g]pteridine-2,4(3H,10H)-dione) core ring and (B) the ribophosphyl chain. Since the photophysical and photochemical behavior of flavins is dominated by the isoalloxazine core, the experimental absorption and emission spectra of different flavins are very similar. In the energy

* Corresponding author. Tel.: +49 211 8113209; fax: +49 211 8113466.
E-mail address: Christel.Marian@uni-duesseldorf.de (C.M. Marian).
URL: http://www.theochem.uni-duesseldorf.de (C.M. Marian).

1010-6030/$ – see front matter © 2008 Elsevier B.V. All rights reserved.
doi:10.1016/j.jphotochem.2008.03.015

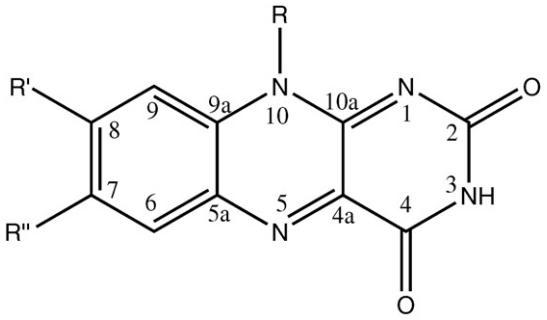

Fig. 1. Chemical structure and labeling of the isoalloxazine core ring of flavins (R=R′=R″=H: isoalloxazine (IA), R=Me,R′=R″=H: 10-methylisoalloxazine (MIA) and R=R′=R″=Me: lumiflavin (LF)).

regime up to 5.5 eV the absorption spectrum of isoalloxazines in solution as well as in the protein environment is dominated by three bands [9,4,6]. In ethanol (EtOH) and the LOV domain, the lowest energy band shows a well-resolved vibronic structure with peaks at 2.63 eV, 2.79 eV, and 2.99 eV (LF in EtOH [9]). In more polar solvents the absorption spectrum is smoothed out. However, the position of this band is hardly affected by the polarity or the proticity of the solvent. In difference to that, the position of the second absorption maximum depends heavily on the environment [10,11]. Experiments in solvents like 1,4-dioxane, 1,2-dichloroethane and acetonitrile confirm that the rising polarity has no major influence on the position of that band. The noticeable red shift of that transition band in solvents like methanol, ethanol, and water shows that the proticity of the solvent plays a more important role [10,9].

The photophysical behavior of different flavins has been the matter of several recent quantum chemical investigations [12–14,10,15,16]. Spin–orbit coupling has been taken into account for the primary step of the photocycle by Climent et al. [13] while Zenichowski et al. [16] have investigated spin–orbit coupling in connection with the adduct formation. In this work, the absorption spectra of the three flavin related compounds isoalloxazine (IA), 10-methylisoalloxazine (MIA), and lumiflavin (LF) (see Fig. 1) are investigated. For MIA, the impact of solvent effects (in water and acetonitrile) on the vertical singlet and the triplet excited energies is evaluated. For all compounds, relaxation pathways after electronic excitation in the vacuum and aqueous solution are studied, taking spin–orbit coupling into account. For IA, intersystem crossing rate constants have been computed, taking both direct and vibronic spin–orbit coupling into account. On this basis the accessibility of the above mentioned ISC channels in water and vacuum is discussed.

2. Methods and computational details

Geometry optimizations of the ground state and low-lying electronically excited states of three isoalloxazines were carried out at the level of density functional theory (DFT) using the TURBOMOLE 5.7[17] program package. For all calculations we employed the standard TZVP basis set from the TURBOMOLE library. The B3LYP functional [18,19] as implemented in TURBOMOLE 5.7 was used for optimizing the geometries. C_s symmetry constraints were imposed on the ground and excited state geometries of all molecules. The cartesian coordinate system was chosen in a way that the *xy* plane coincides with the molecular plane. For the optimization of the electronically excited singlet and triplet state geometries time-dependent DFT [20] (TDDFT) was employed. To ensure that the resulting geometries correspond to true minima of the potential energy hypersurface (PEH), harmonic vibrational frequencies were calculated numerically with the program SNF [21]. Zero-point vibrational energy corrections (ZPVE) were scaled by a factor of 0.9614 as recommended for the B3LYP functional [22].

Vertical electronic excitation energies and dipole moments were obtained from subsequent single-point calculations using the combined density functional theory/multi-reference configuration interaction (DFT/MRCI) method of Grimme and Waletzke [23]. This approach represents an effective means to obtain spin-restricted electronic spectra for organic systems with errors typically less than 0.2 eV. The principle idea is to include major parts of dynamic electron correlation by DFT whereas static electron correlation effects are taken into account by short MRCI expansions. This MRCI expansion is built up in a one-particle basis of Kohn–Sham orbitals employing the BHLYP functional [24,25]. For effectivity reasons and to avoid double-counting of the dynamic correlation, the MRCI expansion is kept short by extensive configuration selection. Furthermore, the 1s electrons of carbon, nitrogen, and oxygen constitute a frozen core. The remaining valence electrons were correlated. Virtual orbitals with energies above $2E_H$ were discarded in the DFT/MRCI calculations. For all geometries we calculated ten roots for each of the two irreducible representations A′ and A″ of the C_s symmetry, both for the singlet and triplet manifolds.

Dipole transition matrix elements and oscillator strength were evaluated at the DFT/MRCI level. From these values, fluorescence rates were obtained according to

$$k_F = \frac{4e^2}{3c^3\hbar^4}(E_i - E_f)^3 |\langle f|\vec{r}|i\rangle|^2 \quad (1)$$

Expressing k_F in units of s^{-1}, ΔE in cm^{-1} and $\langle f|\vec{r}|i\rangle$ in atomic units (ea_0) the numerical prefactor becomes 2.0261×10^{-6}.

For the computation of the spin–orbit matrix elements (SOMEs) between the correlated DFT/MRCI wavefunctions we used the spin–orbit coupling kit (SPOCK) [26,27] developed in our laboratory. For reasons of efficiency, the one-center mean-field approximation to the Breit–Pauli Hamiltonian is used for the description of the spin–orbit coupling. This nonempirical effective one-electron operator treats the expensive two-electron terms of the full Breit–Pauli Hamiltonian in a Fock-like manner [28,29]. It has been shown that the accuracy of this approximation lies within better than 5% of the full treatment [30,31].

According to Toniolo and Persico [32,33], it is possible to approximate the Fermi Golden Rule expression for the ISC rate constants k_{ISC} by a summation over rates of transition from the initial level $|i, \mathbf{v} = 0\rangle$ to individual final vibronic levels $|f, \mathbf{v}'\rangle$ in an energy interval of width 2η around the energy $E_{i,\mathbf{v}=0}$. Here, the vectors $\mathbf{v}$ and $\mathbf{v}'$ represent sets of vibrational quantum numbers in all normal modes of the initial (i) and final (f) electronic state, respectively. If we denote the coupling matrix elements driving the radiationless transition by $H^{SO}_{\mathbf{v}=0,\mathbf{v}'}$, the rate constant is obtained as

$$k_{ISC}(i \rightsquigarrow f) = \frac{2\pi}{\hbar\eta} \sum_{|E_{f,\mathbf{v}'} - E_{i,\mathbf{v}=0}| < \eta} |H^{SO}_{\mathbf{v}=0,\mathbf{v}'}|^2. \quad (2)$$

$H^{SO}_{\mathbf{v}=0,\mathbf{v}'}$ can be expanded in a Taylor series in the variables $\{q_\kappa\}$, the normal coordinates, around some reference point $\mathbf{q}_0$ [34] which we have chosen to coincide with the minimum of the S_1 state.

$$H^{SO}_{\mathbf{v}=0,\mathbf{v}'} = \langle i|\hat{\mathcal{H}}_{SO}|f\rangle\Big|_{\mathbf{q}_0=0}\langle \mathbf{v}=0|\mathbf{v}'\rangle + \sum_\kappa \left(\frac{\partial}{\partial q_\kappa}\langle i|\hat{\mathcal{H}}_{SO}|f\rangle\right)\Bigg|_{\mathbf{q}_0=0}$$
$$\langle \mathbf{v}=0|q_\kappa|\mathbf{v}'\rangle + O(|\mathbf{q}|^2) \quad (3)$$

The first term on the right-hand side of Eq. (3) is a purely electronic matrix element and is denominated direct spin–orbit coupling in the following, whereas the term in the second line of Eq. (3) represents the first-order derivative coupling and is named vibronic spin–orbit coupling.

Rate constants for inter-system crossing from the S_1 state to the three sublevels of the T_1 and T_2 state, respectively, were calculated taking both direct and vibronic spin–orbit coupling into account. According to El-Sayed's rule, SOME between $(\pi \rightarrow \pi^*)$ and $(n \rightarrow \pi^*)$ states are in general much larger than SOME between two $(\pi \rightarrow \pi^*)$ states. Thus, the Condon approximation will yield ISC rate constants that are much slower for $(\pi \rightarrow \pi^*) \rightsquigarrow (\pi \rightarrow \pi^*)$ processes than for $(\pi \rightarrow \pi^*) \rightsquigarrow (n \rightarrow \pi^*)$ processes. As recent studies by Tatchen et al. [35] have shown, vibronic spin–orbit coupling enhances the ISC rate constants between two $(\pi \rightarrow \pi^*)$ states in psoralen. Therefore, a Herzberg–Teller type expansion of spin–orbit coupling around the $^1(\pi \rightarrow \pi^*)$ state minimum (Eq. (3)) was carried out, taking the first-order derivatives of the spin–orbit interaction with respect to *out-of-plane* (*oop*) normal mode coordinates into account. When the molecular geometry is distorted in this way, $(\pi \rightarrow \pi^*)$ and $(n \rightarrow \pi^*)$ states are able to interact and become mixed. This can qualitatively be seen as an intensity borrowing from the much faster $(\pi \rightarrow \pi^*) \rightsquigarrow (n \rightarrow \pi^*)$ process.

The calculations of the ISC rate constants were performed using the VIBES program [36]. The first-order derivatives of the SOME were calculated numerically by finite difference techniques as described in Ref. [35]. The rate constants were calculated for the smallest flavin compound (isoalloxazine) only, for efficiency reasons. In isoalloxazine there are in total 60 vibrational degrees of freedom. Only totally symmetric vibrational modes can serve as accepting modes. In the calculations we allowed excitations into all 41 accepting modes. When vibronic spin–orbit coupling was taken into account, between 8 and 19 *oop* vibrational modes were used as coupling modes. (For further details on the choice of computational parameters see Electronic Supplementary Material (ESM).)

To estimate spectral shifts due to electrostatic interaction in polar solvents we employed the conductor-like screening model (COSMO) which is implemented in the TURBOMOLE package [37,38]. Dielectric constants of $\epsilon = 78$ and $\epsilon = 36$ were chosen, [39] corresponding to water and acetonitrile, respectively, at ambient temperatures. When COSMO was applied, the MRCI expansion was built up from the one-particle basis of COSMO optimized Kohn–Sham orbitals. Because of technical reasons, C_1 symmetry had to be used for all calculations involving COSMO. For both singlet and triplet multiplicity 20 roots were computed. Since COSMO cannot properly model hydrogen bonding, the effects of hydrogen bonding in aqueous solution were mimicked by micro-hydration. For this purpose, we placed four water molecules next to the hetero atoms of the isoalloxazine ring and optimized the ground state without symmetry constraints. In a last approach, the two previous models were combined.

3. Results and discussion

In this section the minimum nuclear arrangements of the ground state as well as the lowest-lying excited states of IA, MIA, and LF and the corresponding vertical electronic spectra are presented. The energetic order of the states is sensitive to the nuclear geometry and typically more than one minimum is found on a particular PEH. This situation is known for various molecules [40,41]. Here, the vertical order of the excited states does not correspond to their adiabatic order. To avoid confusion, we use two different nomenclatures to designate pure multiplicity states: S1, S2, ..., T1, T2, ... denominate *electronic structures* in their energetic order at the ground state minimum geometry. The nomenclature $S_1, S_2, \ldots, T_1, T_2, \ldots$, refers to the actual order of *electronic states* at a given geometry. At the ground state equilibrium geometry, the two nomenclatures are identical, of course.

Table 1
IA, MIA, and LF: selected ground-state geometry bond lengths [pm] and experimental (X-ray) data of MIA [42]

	IA	MIA	LF	(Exp.)
N(1)—C(2)	138.4	138.1	138.0	136.0(5)
C(2)—N(3)	141.8	141.4	141.4	140.8(5)
N(3)—C(4)	138.1	137.9	137.9	135.4(5)
C(4)—C(4a)	150.1	150.2	150.0	148.5(5)
C(4a)—N(5)	129.2	129.0	129.3	129.5(5)
N(5)—C(5a)	137.3	136.9	136.6	136.6(5)
C(5a)—C(6)	140.6	140.5	140.5	141.8(5)
C(6)—C(7)	137.9	137.8	138.0	136.8(6)
C(7)—C(8)	140.4	140.1	142.1	139.5(6)
C(8)—C(9)	138.3	138.4	138.8	138.8(6)
C(9)—C(9a)	139.9	140.3	140.1	139.2(5)
C(9a)—N(10)	137.5	138.6	138.5	139.0(5)
N(10)—C(10a)	136.8	138.2	138.2	136.9(5)
C(10a)—N(1)	129.6	129.9	130.1	131.9(5)
C(5a)—C(9a)	141.6	141.9	141.5	141.8(5)
C(4a)—C(10a)	146.3	146.2	146.1	146.6(5)
C(10)—R	101.2	146.8	146.7	148.8(5)
C(2)—O	121.0	121.1	121.2	121.6(5)
C(4)—O	121.0	121.0	121.1	121.7(5)

Atomic labels are displayed in Fig. 1. Estimated experimental uncertainties are given in parentheses.

3.1. Gas phase

3.1.1. Ground state geometry and vertical excitation spectrum of IA, MIA, and LF

The DFT optimized ground state (S0) geometry of MIA is displayed in Fig. 2. An overview over the most important structural parameters of IA, MIA, and LF can be seen in Table 1. Experimental data for crystalline 10-methylisoalloxazine is available [42] and shows good agreement with the results of our calculations. A comparison of MIA with IA and LF shows that methylation has only minor influence on the geometry. As expected, the addition of a methyl group at N(10) position shows a widening of the C(9)—N(10) and the N(10)—C(10a) bonds. Methylation at C(7) and C(8) position shows a remarkable widening only of the C(7)—C(8) bond by about 2.0 pm which can mainly be explained by sterical effects.

An overview of the vertical DFT/MRCI excitation energies of IA, MIA, and LF in the vacuum can be seen in Table 2. To aid the discussion, the shape and ordering of relevant molecular frontier orbitals of MIA are depicted in Fig. 3. The highest occupied molecular orbital (HOMO) shows electron density mainly at the benzene part of the isoalloxazine ring and the N(1) atom. In contrast, the lowest unoccupied MO (LUMO) shows an increased electron density in the region of the C(4)—C(4a) and C(4a)—C(10a) bonds where the wave function exhibits binding character and in the region of the C(4a)—N(5) where the wave function amplitudes have opposite sign and thus are antibonding. The two MOs, n_{O1} and n_{O2}, are mainly the minus and plus linear combinations of the in-plane lone pairs belonging to the two oxygen atoms. The same principle applies for the two MOs, n_{N1} (not shown) and n_{N2}. The shape of the molecular orbitals of IA and LF hardly differs from the orbitals shown here. It is noticeable that the HOMO and LUMO are very similar for various quantum chemical treatments [15,16,13,12]. For the SAC-CI treatment [12] the ordering of the *n*-MOs changes mainly due to the usage of Hartree–Fock (HF) orbitals.

Unfortunately, there is no experimental gas phase spectrum available for comparison. The comparison with experimental absorption maxima will be postponed to Section 3.2 where results including a solvent model are presented.

In agreement with previous CASPT2, [13] SAC-CI, [12] and TDDFT [14,10,15,16] studies all three experimentally observed bands of the absorption spectrum of flavins can be assigned to $(\pi \rightarrow \pi^*)$ transitions. In the singlet manifold, the lowest-lying excited state is

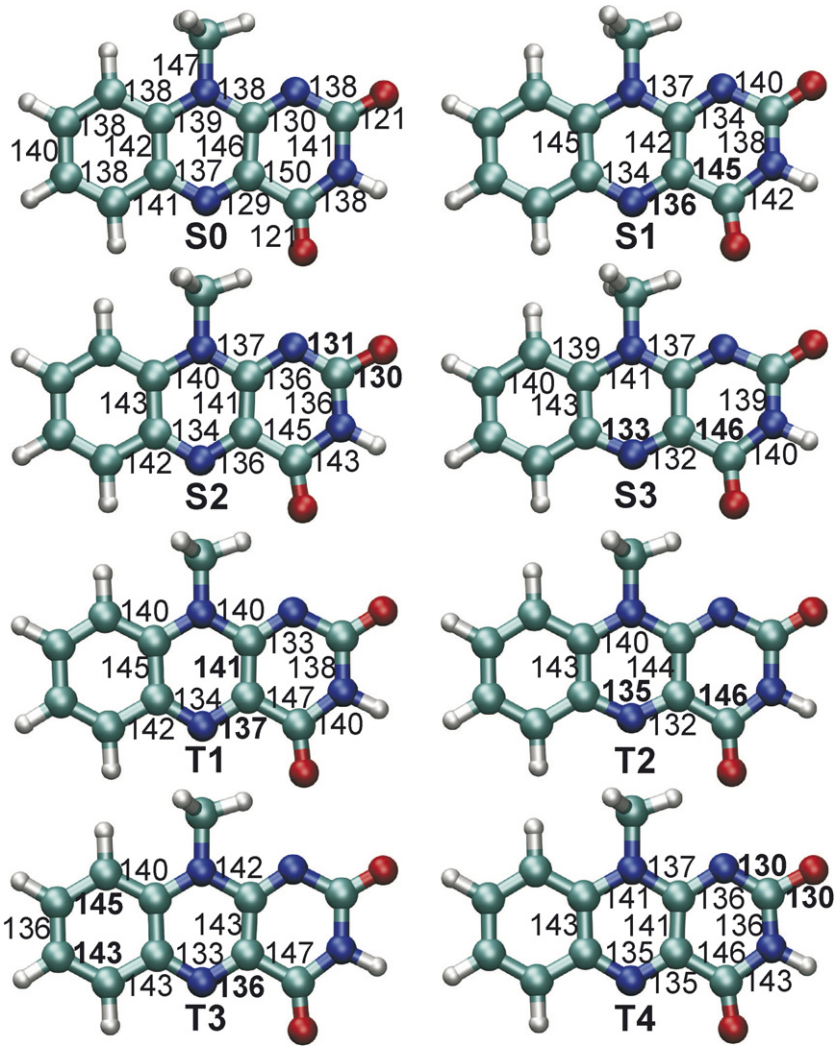

Fig. 2. MIA: TDDFT equilibrium structures of excited states in comparison with the ground-state geometry. (B3LYP,TZVP) All bond lengths in pm, only changes larger than 1 pm with respect to the S0 geometry are shown.

Table 2
IA, MIA, and LF: vertical singlet and triplet excitation energies ΔE [eV] in comparison with recent quantum chemical calculations

State		Electronic structure (MIA)	ΔE					$f(r)$ MIA	μ MIA
			IA [a]	MIA [a]	LF [a]	IA [b]	LF		
S_0	$1^1A'$	(0.95) Ground state	0.00					0.0000	8.20
S_1	$2^1 1A'$	$(0.83)\ \pi_H \rightarrow \pi^*_L$	3.03	3.00	2.94	3.09	2.46 [c], 3.04 [d]	0.2849	9.75
S_2	$1^1A''$	$(0.44)\ n_{O2} \rightarrow \pi^*_L - (0.33) n_{N2} \rightarrow \pi^*_L$	3.16	3.18	3.21	3.75	3.59 [c], 3.09 [d]	0.0025	4.17
S_3	$2^1A''$	$(0.42)\ n_{N2} \rightarrow \pi^*_L + (0.27) n_{O2} \rightarrow \pi^*_L$	3.34	3.33	3.35	3.34	3.18 [c], 3.30 [d]	0.0007	3.95
S_4	$3^1A''$	$(0.59)\ n_{O1} \rightarrow \pi^*_L$	3.90	3.90	3.93	4.43	3.84 [d]	0.0000	3.64
S_5	$3^1A'$	$(0.74)\ \pi_{H-1} \rightarrow \pi^*_L$	3.94	3.93	3.84	4.28	3.84 [c], 3.86 [d]	0.1811	12.97
S_6	$4^1A'$	$(0.74)\ \pi_{H-2} \rightarrow \pi^*_L$	4.05	4.07		4.69	–	0.0350	1.07
⋮	⋮	⋮	⋮	⋮	⋮	⋮	⋮	⋮	⋮
S_9	$6^1A'$	$(0.56)\ \pi_H \rightarrow \pi^*_{L+1} - (0.10) \pi_H \rightarrow \pi^*_{L+2}$	4.86	4.84	4.77	5.00	4.55 [c], 4.91 [d]	0.6275	7.76
S_{10}	$7^1A'$	$(0.37)\ \pi_H \rightarrow \pi^*_{L+2} + (0.17) \pi_H \rightarrow \pi^*_{L+1}$	5.01	5.00	4.91	5.37	4.86 [c]	0.1753	7.41
T_1	$1^3A'$	$(0.85)\ \pi_H \rightarrow \pi^*_L$	2.31	2.30	2.24	2.51	–	–	8.19
T_2	$1^3A''$	$(0.59)\ n_{N2} \rightarrow \pi^*_L - (0.14) n_{O2} \rightarrow \pi^*_L$	2.85	2.87	2.90	2.97	–	–	7.03
T_3	$2^3A'$	$(0.76)\ \pi_{H-1} \rightarrow \pi^*_L$	3.12	3.08	3.05	–	–	–	12.38
T_4	$2^3A''$	$(0.55)\ n_{O2} \rightarrow \pi^*_L$	3.18	3.20	3.21	3.70	–	–	1.65

In addition the dominant excitations, c^2-values, oscillator strengths $f(r)$ and dipole moments μ [Debye] of MIA are given.

[a] DFT/MRCI(TZVP), this work.

[b] CASPT2(6-31G(d)), Ref. [13].

[c] SAC-CI(D95V(d)), Ref. [12].

[d] TDDFT(B3LYP/6-31G(d)), Ref. [16].

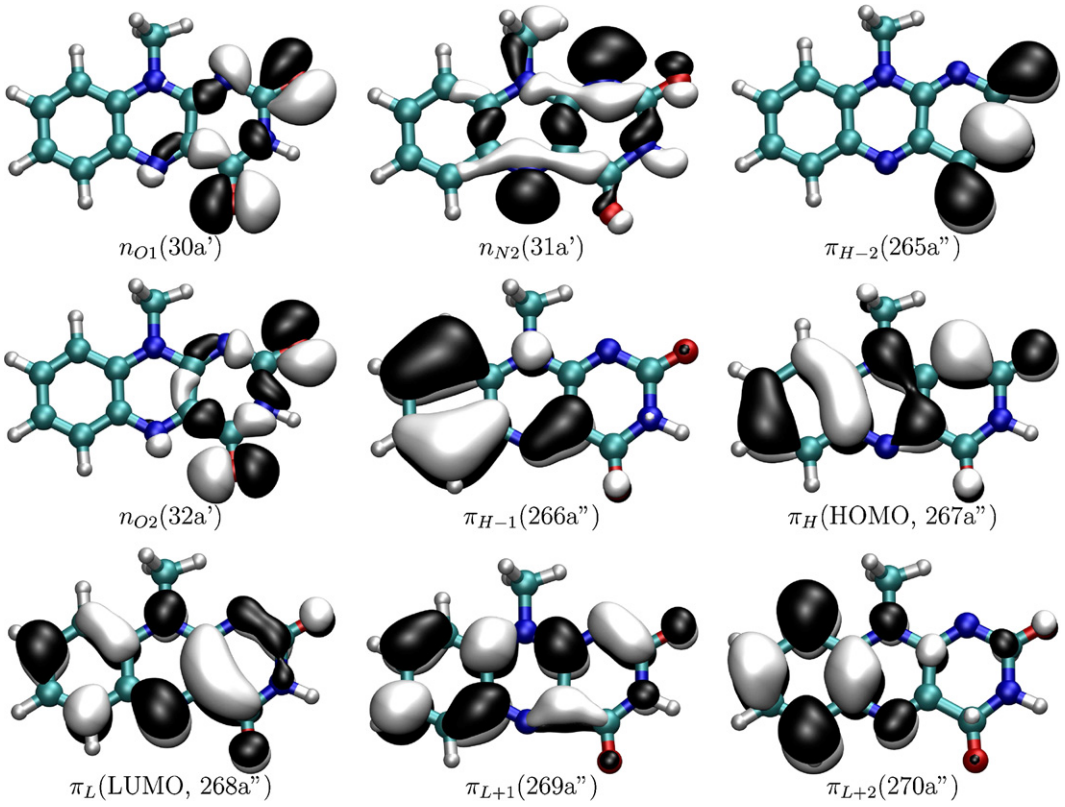

Fig. 3. MIA: Frontier orbitals at the optimized ground-state (S0) geometry (isovalue = 0.3).

dominated by the ($\pi_H \rightarrow \pi^*_L$) (HOMO–LUMO) transition. With an oscillator strength of 0.287 this transition can be assigned to the lowest energy band in the experimental spectrum. For IA, Climent et al. [13] find a CASPT2 energy of 3.09 eV which is very similar to our finding of 3.03 eV. In case of LF the most recent TDDFT treatment [16] has found an energy of 3.04 eV which is in good agreement with the DFT/MRCI and experimental energies. In contrast, the vertical SAC-CI energies for this transition are lower by 0.33 eV. The second excited ^{1}A′ state (S_5) can be assigned to the second visible band in the spectrum. This state is mainly dominated by the ($\pi_{H-1} \rightarrow \pi^*_L$) transition. Its oscillator strength of 0.181 is somewhat smaller than for the first optically bright transition. The vertical CASPT2 excitation energy for IA is much higher (4.28 eV) than our value of 3.94 eV. For LF our DFT/MRCI, the SAC-CI and the TDFFT results all show similar values. The third experimentally observed band of the absorption spectrum can be assigned to the sixth excited ^{1}A′ state (S_9) state. This state is represented by a minus linear combination of the two excitations ($\pi_H \rightarrow \pi^*_{L+1}$) and ($\pi_H \rightarrow \pi^*_{L+2}$), with approximately 56% contribution from the first excitation and only 11% from the second excitation. With an oscillator strength of 0.628 it is the strongest transition in the energy regime up to 5.5 eV. The following excited state is the corresponding plus linear combination with only 17% contribution from the ($\pi_H \rightarrow \pi^*_{L+1}$) excitation and 37% from the ($\pi_H \rightarrow \pi^*_{L+2}$) excitation. With 0.175 the oscillator strength of this 7^1A′ state is much weaker than for the 6^1A′ state, hinting that it is the ($\pi_H \rightarrow \pi^*_{L+1}$) excitation that is optically bright. For LF the multi-reference character of these two states is more pronounced (6^1A′ state with 42% and 25%, 7^1A′ state with 32% and 29%), thus the oscillator strengths of the two states becomes more even (6^1A′ state with 0.491 and 7^1A′ state with 0.346). The vertical CASPT2 excitation energies for IA are (much) higher (5.00 eV and 5.37 eV) than our values of 4.86 eV and 5.01 eV. For LF the SAC-CI of the 6^1A′ state is by 0.22 eV lower than our value of 4.77 eV, while the TDDFT result is 0.14 eV higher. For the 7^1A′ state our DFT/MRCI and the SAC-CI results show similar values.

Contrary to the low-lying (partly) visible $^1(\pi \rightarrow \pi^*)$A′ states which have been discussed quite homogeneously in the literature, the description of the $^1(n \rightarrow \pi^*)$ states differs significantly in the different quantum chemical treatments. Between the first and second visible band we find three $^1(n \rightarrow \pi^*)$ states with small or evanescent oscillator strength. The first ^{1}A″ state is represented by a minus linear combination of the two excitations ($n_{O2} \rightarrow \pi^*_L$) and ($n_{N2} \rightarrow \pi^*_L$), where both c^2-values are quite similar. With an excitation energy ranging between 3.16 eV and 3.21 eV in the three isoalloxazines IA, MIA,and LF this state lies up to 0.25 eV above the first visible 2^1A′ state. A close proximity or even a state flip, as observed for TDDFT treatments, [14,10,15,16] is not found with DFT/MRCI, supporting a similar conclusion drawn by Neiss et al. [15] on the basis of DFT/MRCI calculations employing a smaller basis set. The second ^{1}A″ state is the corresponding plus linear combination with approximately 42% contribution from the ($n_{N2} \rightarrow \pi^*_L$) excitation and only 27% from the ($n_{O2} \rightarrow \pi^*_L$) excitation. The vertical DFT/MRCI excitation energies of 3.33–3.35 eV for the three isoalloxazines agree with the TDDFT value for LF. A comparison of the energies and dominant contributions of these two states with those of CASPT2 and SAC-CI calculations shows that in the latter treatments no multi-reference character is reported. Furthermore, the order of states is flipped with respect to our results, with the ($n_{N2} \rightarrow \pi^*_L$) excitation as the first ^{1}A″ state and the ($n_{O2} \rightarrow \pi^*_L$) excitation heavily blue-shifted. Reasons for this behavior can be seen in the different energetic order of the MOs (SAC-CI, [12] see above) and in an insufficiently large CAS space. According to Climent et al. [13] only one n-orbital per state was included into the active space for the calculation of the ($n \rightarrow \pi^*$) states. By that particular choice of the active space a mixing of the ($n_N \rightarrow \pi^*_L$) and ($n_O \rightarrow \pi^*_L$) excitations as found here is excluded. The third ^{1}A″ state is dominated

by the single excitation ($n_{O1} \rightarrow \pi_L^*$). With an excitation energy of 3.84–3.94 eV it lies in close proximity to the second visible state ($3^1A'$).

As in the singlet case, the lowest-lying triplet excited state is dominated by the ($\pi_H \rightarrow \pi_L^*$) (HOMO–LUMO) transition. The excitation energy of the $1^3A'$ state ranges between 2.24 eV and 2.31 eV, clearly below the corresponding singlet state. The second excited triplet (T_2) state is the minus linear combination of the two excitations ($n_{O2} \rightarrow \pi_L^*$) and ($n_{N2} \rightarrow \pi_L^*$). In contrast to the corresponding singlet state the latter excitation dominates with a c^2-value of 58.7. For all investigated isoalloxazines this $1^3A''$ state also lies below the S_1 states in the vertical excitation spectrum. The T_3 state exhibits ($\pi \rightarrow \pi^*$) character with the ($\pi_{H-1} \rightarrow \pi_L^*$) excitation as the leading conformation. In the vertical excitation spectra of the isolated isoalloxazines the T_3 state is situated energetically between the S_1 and S_2 state. (For further discussion see Section 3.1.3.) The following triplet state (T_4) is dominated by the ($n_{O2} \rightarrow \pi_L^*$)transition. In difference to the corresponding state in the singlet manifold, the multi-reference character is much less pronounced.

As our calculations show, the low-lying excitation energies for IA, MIA, and LF are very similar. In the following we therefore, if not stated otherwise, only discuss MIA.

3.1.2. Excited state geometries and adiabatic transition energies of MIA

For the calculation of all excited states the C_s-symmetry constraint has been retained. The geometries are depicted in Fig. 2 and the electronic excitation energies calculated with DFT/MRCI at the respective geometries can be seen in Fig. 4. Numerical values of the adiabatic excitation energies are collected in Table 3.

Table 3
MIA: adiabatic singlet and triplet DFT/MRCI excitation energies ΔE_{adia} [eV], scaled zero-point vibrational energy corrections (ZPVE) [eV] of low-lying excited states

Geometry	ΔE_{adia}	PEH	ZPVE
S1	2.69	S_1	−0.08
S2	2.90	S_1	−0.07
S3	2.92	S_1	−0.13
S5	3.47 [a]	S_3	–
T1	2.06	T_1	−0.11
T2	2.58	T_2	−0.04
T3	2.79	T_2	−0.11
T4	2.89	T_2	–

[a] Adiabatic excitation energy at the T3 geometry (see text for explanation).

3.1.2.1. S1 and T1 electronic structures. We obtaina minimum nuclear structure for the ($\pi \rightarrow \pi^*$) excited S1 state in which the C(4a) —N(5) bond is elongated by 6.7 pm and the C(4) —C(4a) and C(4a) —C(10a) bonds are shortened by 4.9 pm and 3.8 pm, respectively. This finding is in good agreement with those of Ref. [13,12] and corresponds to the change of nonbonding character of the π_H orbital in that region to an antibonding (C(4a) —N(5)) and bonding (C(4) —C(4a), C(4a) —C(10a)) character in π_L. At the level of TDDFT (B3LYP), this structure only presents a saddle-point on the S_1 PEH. One imaginary frequency ($\tilde{\nu}_1 = i150\,cm^{-1}$) is obtained. It corresponds to an A″-symmetric normal mode which can be described as a mixture of an *oop* deformation of the N(1) and O(2) atoms of the ring and a rotation of the 10-methyl group. We performed a calculation of the TDDFT and DFT/MRCI energies of the S_1 following the distortion along the imaginary A″ normal mode. While TDDFT exhibits an extremely shallow double minimum potential

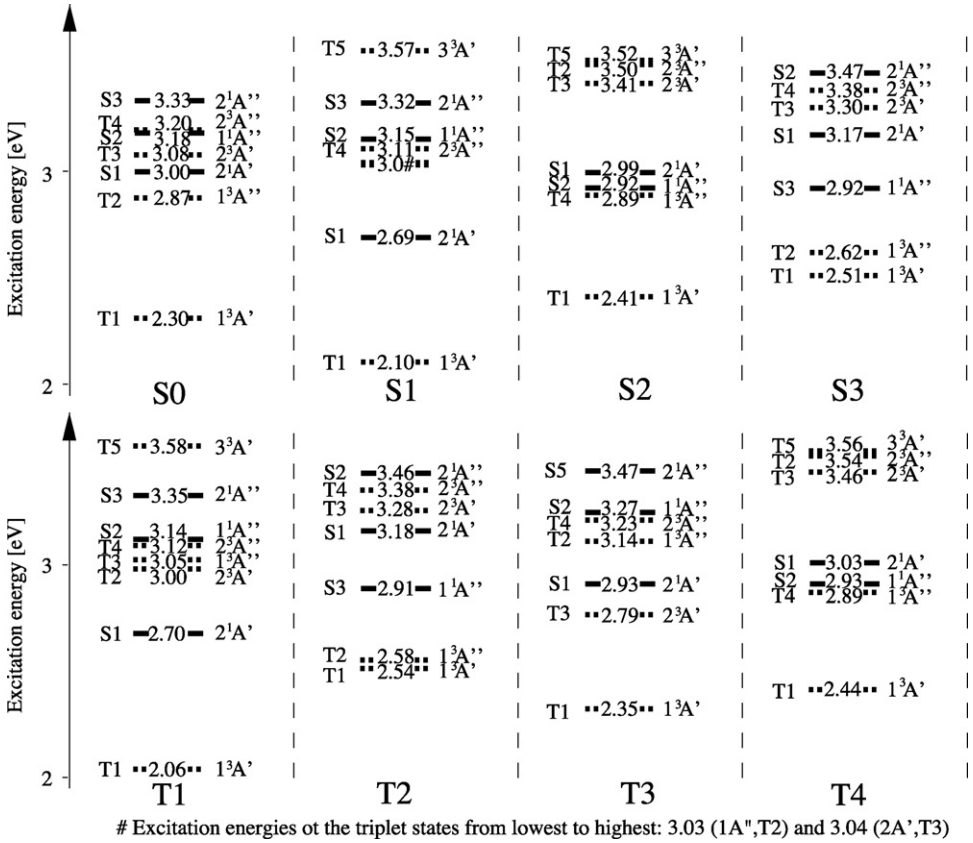

Fig. 4. MIA: Electronic excitation energies (DFT/MRCI, [eV]) at various excited state geometries. For a better comparability, the electronic ground state energy at the S0 geometry has been chosen as the common origin.

well, DFT/MRCI clearly favors the C_s-symmetric structure. This phenomenon has been encountered before in psoralen, cytosine, and thiophene [43,40,41] and is considered an artifact of the TDDFT (B3LYP) method. This imaginary mode can also be observed in LF and IA.

From an energetic point of view, the relaxation effects on the S_1 state are moderate. Its adiabatic excitation energy amounts to 2.69 eV, corresponding to a stabilization by 0.34 eV. At the same time the electronic ground state is destabilized by 0.40 eV yielding a vertical emission energy of 2.28 eV. Due to the small energy difference, the rate of fluorescence to the ground state, calculated at the S_1 minimum, is rather low ($k_F \sim 5 \times 10^7\ s^{-1}$). The experimental rate of fluorescence of MIA in 2-methyltetrahydrofuran (77 K) [44] has been measured to be $k_F = 6.5 \times 10^7\ s^{-1}$ and is in excellent agreement with our calculated rate.

The excitation energies of the other low-lying singlet excited states are not much affected by the geometry relaxation. It is interesting to note that the second excited triplet state is blue-shifted to 3.03 eV at the S1 minimum and is thus located above the S_1, meaning that during the relaxation from the Franck–Condon (FC) region an intersection between the S_1 and T_2 PEH occurs. The crossing between singlet and triplet PEHs as observed here could serve as a funnel for the population of the triplet manifold (see Section 3.1.3).

The geometry of the T1 state is very similar to that of the S1 state. The widening of the C(4a) —N(5) and shortening of the C(4a) —C(10a) bond are more pronounced than at the S1 geometry. This similarity is also reflected in the adiabatic excitation energies. The adiabatic excitation energy of the T_1 state amounts to 2.06 eV in the gas phase.

3.1.2.2. S2 and T4 electronic structures. The computed structure for the ($n \rightarrow \pi^*$) excited S2 state is mainly influenced by the pronounced stretching of the C(2) —O(2) bond by 9.4 pm and the shortening of the N(1) —C(2) bond by 7.7 pm. This is in excellent accordance to the promotion of electron density from the n_{O2} orbital into the LUMO. Contrary to the ground state geometry the electron density of this *n* orbital is primarily localized at the O(2). Furthermore the C(4a) —N(5) bond is elongated by 6.6 pm and the C(4) —C(4a) and C(4a) —C(10a) bonds are shortened by 5.1 pm and 5.2 pm, respectively. At the level of TDDFT (B3LYP), this structure constitutes a minimum on the S_1 PEH. At this point of coordinate space the reverse ordering of the states is corroborated by the DFT/MRCI calculations. The S1 and S2 states are very close in energy ($\Delta E = 0.07$ eV) at this geometry, though. It is anticipated therefore that strong vibronic coupling may occur in the gas phase. According to the model by Lim [45] the proximity effect between a $^1(\pi \rightarrow \pi^*)$ and a $^1(n \rightarrow \pi^*)$ can lead to substantial radiationless decay of the $^1(\pi \rightarrow \pi^*)$ population by internal conversion to the ground state mediated by the $^1(n \rightarrow \pi^*)$ state. Experimentally the S2 state has never been observed, because of the low oscillator strength. The geometry of the T4 state, i.e., the triplet state corresponding to the S2 electronic structure, is very similar to the S2 geometry. It constitutes a minimum on the T_2 PEH, located energetically only slightly below the S2 minimum.

3.1.2.3. S3 and T2 electronic structure. We obtain a nuclear structure for the ($n \rightarrow \pi^*$) excited S3 state where the C(4) —C(4a) and C(5) —C(5a) bonds are shortened by 4.0 pm and 3.9 pm, respectively. At the TDDFT (B3LYP) level this structure is found to be a saddle point on the S_1 PEH. One imaginary frequency ($\bar{\nu}_1 = i43$) is found. This corresponds to an A″-symmetric normal mode which can be described as a mixture of an *oop* deformation of the ring and a rotation of the 10-methyl group. A subsequent calculation of the DFT/MRCI and TDDFT (B3LYP) energies along the distortion of this imaginary normal mode shows the same picture as for the A″-symmetric imaginary normal mode at the S1 geometry, i.e., the *oop* deformation is an artifact of the TDDFT (B3LYP) treatment.

With regard to the energy, the relaxation effect on the optimized S3 state is stronger than for the S2 structure and yields an adiabatic excitation energy of 2.92 eV. As in TDDFT (B3LYP) this electronic state constitutes a local minimum on the S_1 PEH.

Again, the geometry and the excitation energy of the corresponding triplet state (T2) show no major difference. The optimized T2 state is red-shifted close to the T1 state at this geometry (difference around 0.04 eV) but the two states still retain the same order as at the ground state geometry.

3.1.2.4. S5 and T3 electronic structures. Due to root flipping the minimum nuclear arrangement of the ($\pi \rightarrow \pi^*$) S5 state could not be computed and only that of the corresponding triplet state is available. The computed minimum nuclear structure of the T3 state is characterized by the elongation of the C(4a) —N(5), C(6) —C(7), and C(8) —C(9) bonds by 7.0 pm, 5.5 pm, and 6.3 pm, respectively, and the shortage of the C(7) —C(8) bond by 4.2 pm. Looking at the π_{H-1} and π_L orbitals, the geometry shifts are in accordance to the change of character from bonding to antibonding for the three elongated bonds and vice versa for the shortened bond. The geometry relaxation leads to a stabilization by 0.33 eV and yields an adiabatic excitation energy of 2.79 eV. At the DFT/MRCI level this state exhibits a local minimum on the T_2 PEH. A calculation of the harmonic normal modes at TDDFT level yields a true minimum. The corresponding singlet state S5 is found to be on the S_3 PEH. Since it was not possible to optimize the S5 geometry, the adiabatic excitation energy of the S5 at the optimized T3 geometry is used. This is justified by the observation that for all other pairs of singlet and triplet states the adiabatic excitation energies at the two respective geometries are less than 0.05 eV apart.

3.1.3. Inter-system crossing

As mentioned in the introduction, the photochemical reaction of FMN with a nearby cysteine residue of the LOV domain takes place in an intermediate triplet state. It is accepted in the literature that this state is the first excited triplet state and that triplet formation happens very efficiently at a timescale of nanoseconds after absorption of a photon [46]. Inspection of Fig. 4 shows that, from an energetic point of view, the T1 and T2 are possible candidates for efficient ISC from S1 in the gas phase. As noted above, the energy gap between the S1 and T2 minima is small (0.11 eV). The energetic order of the T_2 and the S_1 PEHs even changes when proceeding from the S0 to the S1 geometry, resulting in an intersection between the two PEHs, which should be easily accessible from the Franck–Condon (FC) region. Since the two crossing PEHs are of ($\pi \rightarrow \pi^*$) and ($n \rightarrow \pi^*$) character, substantial spin–orbit coupling matrix elements between the two states can be expected, and an efficient population transfer to the triplet manifold might be possible.

A path between the S0 and the S1 geometry has been linearly interpolated for all three flavins. In Fig. 5 (top) the DFT/MRCI energies of low-lying states along that path in MIA can be seen. As expected, the crossing of the T_2 and the S_1 PEHs can be reached from the FC region without barrier. The excitation energy amounts to approximately 2.9 eV here. Spin–orbit coupling at the crossing point is substantial, with SOME values of 8.3(9.2) cm^{-1} and 1.9(2.7) cm^{-1} for the *x* and *y* components in MIA(IA), respectively. For LF similar results have been obtained. At CASPT2 level a homologous path has been found by Climent et al. for IA with SOME values between 2 cm^{-1} and 11 cm^{-1} [13].

The results of our evaluation of the rate constants $k_{ISC}(S \rightsquigarrow T)$ for singlet–triplet ISC in IA are summarized in Table 4. A more detailed

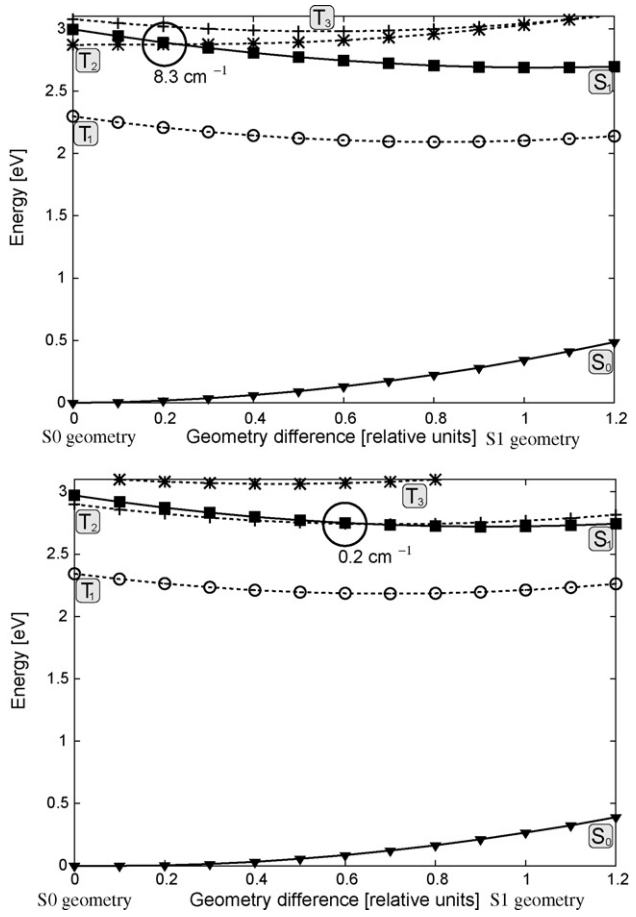

Fig. 5. MIA: DFT/MRCI energies of low-lying states along a linearly interpolated path between the S0 and the S1 geometry for the vacuum (top) and the COSMO environment (bottom). Singlet energy profiles are represented by solid lines, triplet profiles by dashed lines. Triangles symbolize the ground state, stars a ($n \rightarrow \pi^*$) state and circles, squares and plus signs ($\pi \rightarrow \pi^*$)states. For the crossing points the largest components of the spin–orbit coupling matrix elements $\langle T_2|H_{SO}|S_1\rangle$ are given.

overview about the calculations with further information about the parameters used, can be seen in the ESM (Table 2).

Let us first discuss the results of the Condon approximation, i.e., when only direct spin–orbit coupling is taken into account. In this case, only the ISC processes from the zero vibrational level of the S1 ($\pi \rightarrow \pi^*$) state to the vibrational states in the T2 ($n \rightarrow \pi^*$) potential well are fast. Due to the small energy gap between the S1 and T2 minima (which is further reduced due to the higher zero-point vibrational energy in the T2 state) the density of vibrational states in the final T2 potential well is small—far from the ideal situation of a quasi-continuum for which the Fermi Golden Rule was derived. The search interval η therefore had to be rather large. On the other hand, calculated relative energies are always afflicted with uncertainties. To study the sensitivity of the ISC rates with respect to the chosen value of the η parameter and the size of the energy gap, we carried out numerous test calculations the results of which are given in Tables 2 and 5 of the ESM. With the exception of the cases where only very few vibrational levels are found in the search interval, the calculated ISC rates k_{ISC} range between $\sim 1 \times 10^9$ s^{-1} and $\sim 2 \times 10^9\ s^{-1}$ for the $S_1 \rightsquigarrow T_{2x}$ channel. Due to the smaller electronic coupling matrix element (which enters quadratically) the corresponding $S_1 \rightsquigarrow T_{2y}$ ISC rate is calculated to be one order of magnitude smaller.

Tatchen et al. [35] and Perun et al. [47] recently observed that vibronic spin–orbit coupling remarkably enhances the ISC processes between two ($\pi \rightarrow \pi^*$) states. As a result of this Herzberg–Teller type interaction, the rates of the transitions $S_1(\pi{\rightarrow}\pi*) \rightsquigarrow T_{1x,1y}(\pi{\rightarrow}\pi*)$ are increased from $\sim 10^{-2}\ s^{-1}$ to $\sim 10^6\ s^{-1}$, but they cannot compete with the rates involving the respective T_2 levels.

Since the fastest process ($k_{ISC} \sim 10^9\ s^{-1}$) dominates the rate constant, we estimate the ISC from the $S_1(\pi{\rightarrow}\pi*)$ state to the triplet manifold in the gas phase to take place at the timescale of nanoseconds, more than one magnitude faster than the spin-allowed radiative transition to the electronic ground state. This result indicates that after blue light absorption a significant part of excited state population could be transferred into the triplet manifold before the excited state population is depleted by fluorescence or internal conversion.

Table 4
IA: calculated rate constants k_{ISC} [s^{-1}] (right) for ($S_1 \rightsquigarrow T_n$) ISC channels (left) in the vacuum

Channel $i \rightsquigarrow f$	ΔE^{ad}	Direct SO, $\lvert\langle i\rvert\hat{H}_{SO}\lvert f\rangle\rvert_{q0}$	Rate, k_{ISC}
$S_1 \rightsquigarrow T_{1x}$	−0.65	–	3.1×10^6
$S_1 \rightsquigarrow T_{1y}$	−0.65	–	2.3×10^6
$S_1 \rightsquigarrow T_{1z}$	−0.65	0.9×10^{-2}	4.0×10^1
$S_1 \rightsquigarrow T_{2x}$	−0.11	13.7	$\sim 10^9$
$S_1 \rightsquigarrow T_{2y}$	−0.11	6.8	$\sim 10^8$
$S_1 \rightsquigarrow T_{2y}$	−0.11	–	–

Remaining columns: adiabatic electronic energy difference ΔE^{ad} [eV], direct SOME $\lvert\langle i\rvert\hat{H}_{SO}\lvert f\rangle\rvert_{q0}$ [cm^{-1}].

Table 5
MIA: vertical (**v**) and adiabatic (**a**) singlet and triplet DFT/MRCI excitation energies ΔE_{adia} [eV] in comparison with experimental data

Transition		ΔE_{adia}			Experiment		
		Vac.	AcN	H_2O	2MTHF [a]	AcN [b]	H_2O [c]
$S_0 \rightarrow S_1$	**v**	3.00	2.96	2.94	2.88	2.84	2.85
	a	2.69	–	–	2.70, 2.72	–	–
$S_0 \rightarrow S_5$	**v**	3.94	3.80	3.61	3.82	3.78	3.62
	a	3.47 [d]	–	–	3.53	–	–
$S_0 \rightarrow S_9$	**v**	4.86	4.86	4.90	–	4.65	4.70

AcN: acetonitrile, 2MTHF: 2-methyltetrahydrofuran.
[a] Absorption spectrum of 3,10-dimethylisoalloxazine in 2-methyltetrahydrofuran at 300 and 77 K, see Ref. [44].
[b] Absorption maximum in acetonitril, Ref. [11]
[c] Absorption maximum in water, Ref. [11]
[d] Adiabatic excitation energy at the T3 geometry (see text for explanation).

3.2. Solvent effects

As stated above we could not compare our calculated vacuum DFT/MRCI excitation energies with experimental gas phase data, but had to refer to measurements in solution (water and acetonitrile). As described in the introduction, the second visible band of isoalloxazines shows a pronounced solvatochromism. Since solvent effects have a substantial effect on the absorption spectra, they have been taken into account employing three models: (II) a continuum model using COSMO, (III) micro-hydration with four explicit water molecules (see Fig. 6) and (IV) a combination of both. In addition we have carried out COSMO calculations for a dielectric constant of $\epsilon = 36$ corresponding to acetonitrile (AcN).

3.2.1. Vertical excitation energies in water

The excitation energies of MIA in aqueous solution of the models II-IV are displayed and compared to those of the vacuum (I) in Fig. 7. In a simplified picture, the energetic stabilization or destabilization of the ground and excited states in polar solvents is connected to

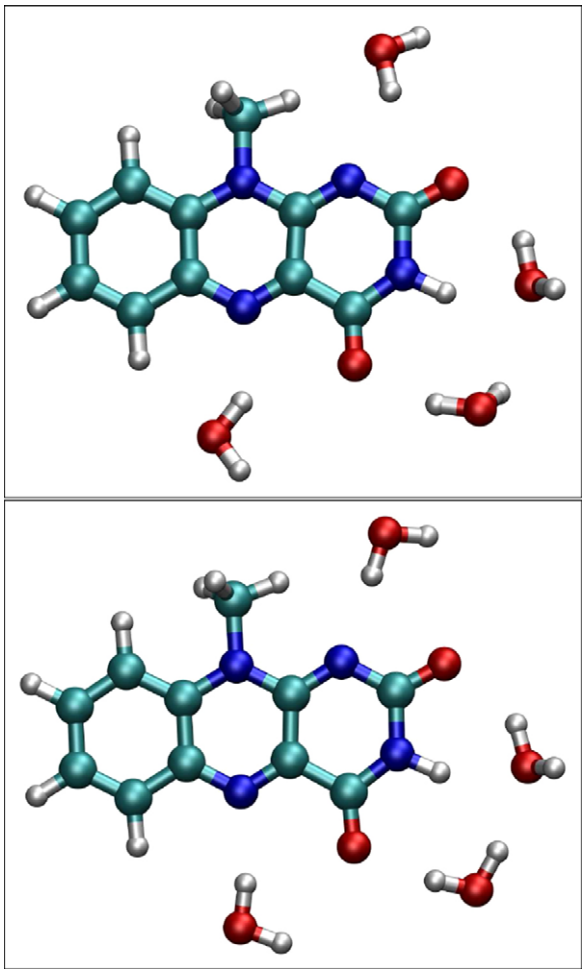

Fig. 6. MIA: Micro-hydrated cluster in the vacuum (top) and with COSMO (bottom).

their dipole moments and the extent of polarization they induce in the surrounding solvent. According to the dipole moments in Table 2, the effect on the excitation energies of the ($\pi_H \rightarrow \pi^*_L$) and ($\pi_H \rightarrow \pi^*_{L+1}$) states should be small while the effect on the ($\pi_{H-1} \rightarrow \pi^*_L$), and ($n \rightarrow \pi^*$) states is expected to be strong.

In agreement with experimental trends and earlier quantum chemical investigations, [12,16] the excitation energies of the first and third visible transitions ($^1(\pi_H \rightarrow \pi^*_L)$ and $^1(\pi_H \rightarrow \pi^*_{L+1})$ states) are hardly affected by solvent effects, while the second visible transition ($^1(\pi_{H-1} \rightarrow \pi^*_L)$ state) is red-shifted by about 0.3 eV due to solvation in water. The vertical excitation energy obtained with our best solvation model (IV), 3.61 eV, agrees excellently with the experimental band maximum of 3.63 eV in neutral aqueous solution at room temperature [44]. It is seen that COSMO alone underestimates the solvent shift of that state. A comparison of the models (II) and (III) shows that a major part of the solvatochromism originates from hydrogen bonding. This finding is in accordance to the observation of Sikorska et al. [10] that the proticity of the solvents plays a more important role for the solvatochromism than the polarity. The corresponding triplet states ($^3(\pi_{H-1} \rightarrow \pi^*_L)$ and $^3(\pi_H \rightarrow \pi^*_L)$) show the same behavior as their singlet counterparts. The $^3(\pi_{H-1} \rightarrow \pi^*_L)$ state is red-shifted by up to 0.3 eV and lies, as soon as solvation is included, below the $^3(n_{N2} \rightarrow \pi^*_L)$ state. As will be seen in Section 3.2.2, these solvent shifts have a large impact on the ISC mechanism.

Within the manifold of ($n \rightarrow \pi^*$)states, the blue-shifts due to solvent effects are more pronounced for the ($n_{O2} \rightarrow \pi^*_L$) states than for the ($n_{N2} \rightarrow \pi^*_L$) states, which is also observed in Ref. [12]. Qualitatively this is easily understood. As shown in Fig. 6, the water molecules form strong hydrogen bonds with the oxygen acceptors. Because of the hydrogen bond interaction these lone-pair orbitals are stabilized. A promotion of one n_{O2} electron to the π^* orbital thus requires significantly more energy. As a result, solvation in water pushes the ($n_{O2} \rightarrow \pi^*_L$) structure, which used to correspond to the S2 structure in the vacuum, energetically far above the S1 $^1(\pi_H \rightarrow \pi^*_L)$ structure and even above the ($n_{N2} \rightarrow \pi^*_L$) structure. A participation of the S2 structure in the radiationless decay of the S1 state is therefore hindered. As for the ($\pi \rightarrow \pi^*$) states, the prediction of solvent effects with COSMO underestimates the spectroscopic shift of the ($n \rightarrow \pi^*$) states. In connection with the relaxation pathway the position of the $^3(n_{N2} \rightarrow \pi^*_L)$ state is of special interest. Due to the pronounced blue-shift for the models with conductor-like screening this state is no longer accessible from the S1 state. If only hydrogen bonding is involved, the $^3(n_{N2} \rightarrow \pi^*_L)$ state is almost degenerate to the $^1(\pi_H \rightarrow \pi^*_L)$ and $^3(\pi_{H-1} \rightarrow \pi^*_L)$ states. In protic systems with low polarity, such as proteins, it is possible that both triplet states could be involved in the ISC mechanism. A closer investigation of these systems is in progress and beyond the scope of this work.

3.2.2. *Inter-system crossing in water*

In order to estimate the impact of the solution on the relaxation pathway, DFT/MRCI calculations have been carried out with model (II) at the same geometries as in Section 3.1.3. In Fig. 5(bottom) the

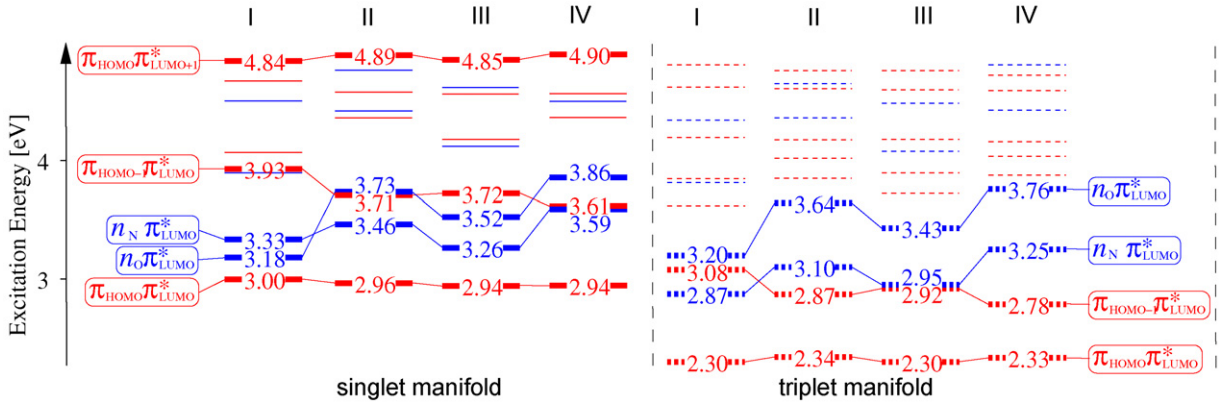

Fig. 7. MIA: Comparison of the vertical excitation energies for the vacuum (I), solvation with COSMO (II), micro-hydration with four explicit water molecules (III), and a combination of the latter (IV).

Table 6
IA: calculated rate constants k_{ISC} [s^{-1}] for ($S_1 \rightsquigarrow T_n$) ISC channels in aqueous solution

Channel $i \rightsquigarrow f$	ΔE^{ad}	Direct SO, $\lvert\langle i\rvert\hat{H}_{SO}\lvert f\rangle\rvert_{q0}$	Rate, k_{ISC}
$S_1 \rightsquigarrow T_{1x}$	−0.56	$< 10^{-3}$	3.6×10^5
$S_1 \rightsquigarrow T_{1y}$	−0.56	$< 10^{-3}$	2.8×10^5
$S_1 \rightsquigarrow T_{1z}$	−0.56	0.9×10^{-2}	1.1×10^2
$S_1 \rightsquigarrow T_{2x}$	−0.12	$< 10^{-3}$	$\sim 10^7$
$S_1 \rightsquigarrow T_{2y}$	−0.12	$< 10^{-3}$	$\sim 10^8$
$S_1 \rightsquigarrow T_{2y}$	−0.12	0.3×10^{-2}	1.1×10^1

For further information see 4.

DFT/MRCI energies of low-lying states along the path can be seen.

As noted above, the $^3(n_{N2} \rightarrow \pi^*_L)$ state is significantly blue-shifted and therefore energetically no longer accessible from low-lying vibrational levels of the S1 state. Due to the strong red-shift, the $^3(\pi_{H-1} \rightarrow \pi^*_L)$ electronic structure (T3) represents the second excited triplet state (T_2) in aqueous solution. Near the S1 minimum, a crossing of the T_2 and the S_1 PEHs takes place without barrier at an excitation energy of about 2.75 eV. Direct spin–orbit coupling at the crossing point is very small. The values for all cartesian components of the SOME in IA are less than 10^{-3} cm^{-1} and indicate a dramatically slower ISC rate than in the vacuum. The impact of vibronic spin–orbit coupling on the rate constant of isoalloxazines is huge.

As shown in Table 6, the rate constants of the $S_1 \rightsquigarrow T_1$ transitions increase from $\sim 10^2$ s^{-1} to $\sim 10^5$ s^{-1} when vibronic interactions are invoked. Nevertheless, they are much too slow to compete with the fluorescence ($k_F \sim 5 \times 10^7$ s^{-1}). The calculated rates of the $S_1 \rightsquigarrow T2$ intersystem crossing are more sensitive to the choice of computational parameters (number of coupling modes, size of the integration interval η, for details see Table 3 of the ESM) than of the $S_1 \rightsquigarrow T_1$ nonradiative transition. For the same reasons as discussed in Section 3.1.3, a search interval width of merely 0.1 cm^{-1} must be considered too small for potential wells lying so close in energy. It is interesting to observe that the rates of the $S_1 \rightsquigarrow T_2$ nonradiative transitions depend markedly on the number of coupling modes employed (see Table 3 of the ESM). In this case it is not sufficient to include the most strongly coupling modes. Astoundingly, but very comforting, the results are quite robust with respect to variations of the energy gap by a few hundred per centimeter, once a search interval of at least 10 cm^{-1} around the initial state is used in the calculations. With a sufficient number of vibrational states within the search interval and all coupling modes involved, the results converge towards k_{ISC} values of the order of $\sim 10^8$ s^{-1}. The experimental rate constants for FMN are $k_{ISC} = 10^8$ s^{-1} in water [4]. Although our theoretical results have to be judged with some reservation due to the fact that the excited state geometries were taken from the gas phase calculations and not relaxed in the presence of the solvent, the comparison with experiment shows that our values are in the right ballpark.

3.2.3. Excitation energies in acetonitrile and comparison with experiment

For acetonitrile solution only model II was employed at the vacuum ground state geometry. As for aqueous solution the excitation energy of the first visible transition ($^1(\pi_H \rightarrow \pi^*_L)$state) is hardly affected by solvation in acetonitrile. For the $2A'$ state the solvent shift amounts to merely 0.04 eV. Our computed vertical excitation energy of 2.96 eV fits well with the experimental band maximum of the absorption spectrum at 2.84 eV. Because of the small solvent shift of the vertical S0 → S1 excitation at the S0 geometry it appears to be save to neglect solvent effects when comparing energies of this electronic structure at other geometries, too. Our calculated gas phase value for the adiabatic S1 energy agrees very well with the experimental band origin of MIA in 2-methyltetrahydrofuran [44]. The vertical emission energy in the vacuum is calculated to be 2.35 eV which is in excellent agreement with experimental fluorescence maxima in acetonitrile and water at room temperature (2.33–2.38 eV) [11]. Due to the lower polarity of the solvent, the red-shift of the second visible transition ($^1(\pi_{H-1} \rightarrow \pi^*_L)$state) is less pronounced than in water. The computed vertical excitation energy of 3.80 eV for the $3^1A'$ state agrees perfectly with the experimental band maximum of the absorption spectrum at 3.78 eV [11]. Our DFT/MRCI value of 3.47 eV shows good agreement with an experimental value of 3.53 eV [44] for the origin of the corresponding absorption band.

In the triplet manifold the order of the four lowest-lying states is retained with respect to the vacuum. In accord with the trends for the S1 state, the T1 state experiences only minor solvent effects. It is therefore not surprising that the experimental origin transition of the T1 phosphorescence at 2.14 eV [44] matches nearly perfectly with our calculated adiabatic T1 excitation energy of 2.06 eV in the vacuum. As their singlet counterparts, the two ($n \rightarrow \pi^*$) states are blue-shifted whereas the $^3(\pi_{H-1} \rightarrow \pi^*_L)$ state (T3) is red-shifted and becomes almost degenerate to the first excited singlet state.

4. Summary and conclusions

We have presented optimized ground-state geometries of isoalloxazine (IA), 10-methylisoalloxazine (MIA), and lumiflavin (LF). A comparison of the structure of MIA with experimental X-ray data reveals very good agreement of the structural parameters. The different states of methylation show only minor influence on the equilibrium geometries, mainly due to steric effects. Also the shape and energetic order of the frontier orbitals is very similar. A comparison of the DFT/MRCI absorption spectra of these three isoalloxazines shows that the vertical excitation energies are very much alike. This fact is in perfect agreement with experiment. To the best of our knowledge, experimental gas phase spectra in the visible and UV regions are not available so that a direct comparison with our calculated excitation energies of the isolated molecules is not possible at the present stage.

For the quantitative evaluation of inter-system crossing (ISC) rate constants, adiabatic excitation energies and vibrational frequencies of several low-lying singlet and triplet excited states have been determined. Our study shows that there are at least three minima on the first excited singlet potential energy hypersurface (PEH) corresponding to the $2^1A'$ (S_1), $1^1A''$ (S_2), and $2^1A''$ (S_3) states in the vertical spectrum.

Solvent effects have been taken into account for MIA with three different models for acetonitrile (COSMO) and water (COSMO, micro-hydration, and a combination of both). In accordance to earlier quantum chemical treatments, all three experimentally visible bands of the absorption spectrum of isoalloxazines could be assigned to ($\pi \rightarrow \pi^*$) transitions. Our calculated vertical excitation energies differ from the corresponding band maxima of the experimentally known absorption spectra by at most 0.2 eV. All models excellently reproduce the red-shift of the second visible $^1(\pi \rightarrow \pi^*)$ transition, observed in experiment and recent quantum mechanical studies. Solvent shifts of the triplet states have been presented in this work for the first time. They are particularly interesting with regard to ISC probabilities.

A linearly interpolated path has been constructed between the Franck–Condon region and the minimum geometry of the first excited $^1(\pi \rightarrow \pi^*)$ state which is responsible for the blue-light absorption. Along this path, DFT/MRCI energies have been calculated for the vacuum and aqueous solution (COSMO). On the basis

of these calculations we suggest possible ISC channels. In both, vacuum and solution, we find a crossing between the S_1 and T_2 PEH along this reaction path. In agreement with earlier theoretical work by Climent et al. [13] a crossing between the $^1(\pi \rightarrow \pi^*)$ (S_1) and $^3(n \rightarrow \pi^*)$ (T_2) states is observed in the isolated flavins. Spin–orbit matrix elements (SOME) between the PEHs are substantial in that region. The minimum of the T_2 state is placed at a slightly lower energy than that of the S_1 state. The combination of favorable Franck–Condon factors between the initially populated S_1 and the T_2 state in the crossing region, substantial electronic spin–orbit coupling and a small energy gap raise the expectation of an efficient ISC. Quantitative ISC rate constants for nonradiative singlet–triplet transitions of flavins have been determined for the first time. We predict the transition to occur at the nanosecond timescale, with the individual rates being $k_{ISC} \sim 10^9\ s^{-1}$ and $k_{ISC} \sim 10^8\ s^{-1}$ for the $S_1 \rightsquigarrow T_{2x}$ and $S_1 \rightsquigarrow T_{2y}$ channels, respectively, in the vacuum. It may thus efficiently compete with or even quench the radiative decay of the S_1 state which is computed to take place at a rate of $k_F \sim 5 \times 10^7\ s^{-1}$. As a further channel for the nonradiative decay of the S_1 state our results suggest internal conversion to the ground state enhanced by the energetic proximity of the first $^1(n \rightarrow \pi^*)$ state.

In aqueous solution the $(n \rightarrow \pi^*)$ states are significantly blue-shifted so that the ISC channel described above for the isolated chromophore is no longer available. Instead, a crossing between the $^1(\pi \rightarrow \pi^*)(S_1)$ and $^3(\pi \rightarrow \pi^*)(T_2)$ states takes place. The SOME is much smaller in this case which at first glance hints at a much smaller ISC rate. However, vibronic spin–orbit coupling increases the latter to $k_{ISC} \sim 10^8\ s^{-1}$. Comparing this rate to the fluorescence rate $k_F \sim 5 \times 10^7\ s^{-1}$ we are lead to the conclusion that in water population transfer into the triplet manifold is still efficient after blue-light absorption, despite the fact that the $^3(n \rightarrow \pi^*)$ PEH cannot be reached. Internal conversion of the S_1 population is suppressed in aqueous solution due to the blue-shift of the lowest $^1(n \rightarrow \pi^*)$ state.

In this work, we propose a consistent model of the photophysical relaxation of flavin after blue-light absorption. In difference to earlier quantum chemical investigations, our work on the photophysics of flavins goes beyond the relaxation in the vacuum [13] or the impact of environmental effects on the vertical absorption spectrum [12,16]. In fact, for the first time the effect of aqueous solution on the relaxation pathway of flavins and ISC rate constants in both environments have been obtained.

What remains to be done is to investigate the photophysical relaxation of the flavin chromophore in the protein environment of the LOV domains. Work in that direction is currently undertaken.

Acknowledgment

Financial support by the Deutsche Forschungsgemeinschaft through SFB663/C1 is gratefully acknowledged.

Appendix A. Supplementary data

Supplementary data associated with this article can be found, in the online version, at doi:10.1016/j.jphotochem.2008.03.015.

References

[1] A. Losi, Photochem. Photobiol. 83 (2007) 1283–1300.
[2] W.R. Briggs, C.F. Beck, A.R. Cashmore, J.M. Christie, J. Hughes, J.A. Jarillo, T. Kagawa, H. Kanegae, E. Liscum, A. Nagatani, K. Okada, M. Salomon, W. Rüdiger, T. Sakai, M. Takano, M. Wada, J.C. Watson, Plant Cell 13 (2001) 993–997.
[3] M. Gomelsky, G. Klug, Trends Biochem. Sci. 10 (2002) 497–500.
[4] J.T.M. Kennis, S. Crosson, M. Gauden, I.H.M. van Stokkum, K. Moffat, R. van Grondelle, Biochemistry 42 (2003) 3385–3392.
[5] W. Holzer, A. Penzkofer, M. Fuhrmann, P. Hegemann, Photochem. Photobiol. 75 (2002) 479–487.
[6] W. Holzer, A. Penzkofer, P. Hegemann, Chem. Phys. 308 (2005) 79–91.
[7] T.E. Swartz, S.B. Corchnoy, J.M. Christie, J.W. Lewis, I. Szundi, W.R. Briggs, R.A. Bogomolni, J. Biol. Chem. 276 (2001) 36493–36500.
[8] M. Salomon, J.M. Christie, E. Knieb, U. Lempert, W.R. Briggs, Biochemistry 39 (2000) 9401–9410.
[9] M. Sung, T.A. Moore, P.-S. Song, J. Am. Chem. Soc. 94 (1972) 1730–1740.
[10] E. Sikorska, I.V. Khmelinskii, D.R. Worrall, J. Koput, M. Sikorski, J. Fluores. 14 (2004) 57–64.
[11] A.J.W.G. Visser, F. Müller, Hel. Chim. Acta 62 (1979) 593–608.
[12] J. Hasegawa, S. Bureekaew, H. Nakatsuji, J. Photochem. Photobiol. A 189 (2007) 205–210.
[13] T. Climent, R. González, M. Merchán, L. Serrano-Andrés, J. Phys. Chem. A 110 (2006) 13584–13590.
[14] E. Sikorska, I.V. Khmelinskii, J. Koput, J.L. Bourdelande, M. Sikorski, J. Mol. Struct. 697 (2004) 137–141.
[15] C. Neiss, P. Saalfrank, M. Parac, S. Grimme, J. Phys. Chem. A 107 (2003) 140–147.
[16] K. Zenichowski, M. Gothe, P. Saalfrank, J. Photochem. Photobiol. A 190 (2007) 290–300.
[17] R. Ahlrichs, M. Bär, H.-P. Baron, R. Bauernschmitt, S. Böcker, N. Crawford, P. Deglmann, M. Ehrig, K. Eichkorn, S. Elliott, F. Furche, F. Haase, M. Häser, C. Hättig, H. Horn, C. Huber, U. Huniar, M. Kattannek, A. Köhn, C. Kölmel, M. Kollwitz, K. May, P. Nava, C. Ochsenfeld, H. Öhm, H. Patzelt, D. Rappoport, O. Rubner, A. Schäfer, U. Schneider, M. Sierka, O. Treutler, B. Unterreiner, M. von Arnim, F. Weigend, P. Weis, H. Weiss, Turbomole (vers. 5.7), University of Karlsruhe (2004).
[18] A.D. Becke, J. Chem. Phys. 98 (1993) 5648–5652.
[19] P.J. Stephens, F.J. Devlin, C.F. Chabalowski, M.J. Frisch, J. Phys. Chem. 98 (1994) 11623–11627.
[20] R. Bauernschmitt, R. Ahlrichs, Chem. Phys. Lett. 256 (1996) 454–464.
[21] C. Kind, M. Reiher, J. Neugebauer, SNF Version 2.2.1: A Program Package for Numerical Frequency Analyses, Universität Erlangen, 1999–2002.
[22] A.P. Scott, L. Radom, J. Phys. Chem. 100 (1996) 16502–16513.
[23] S. Grimme, M. Waletzke, J. Chem. Phys. 111 (1999) 5645–5655.
[24] A.D. Becke, J. Chem. Phys. 98 (1993) 1372–1377.
[25] C. Lee, W. Yang, R.G. Parr, Phys. Rev. B 37 (1988) 785–789.
[26] M. Kleinschmidt, J. Tatchen, C.M. Marian, J. Comput. Chem. 23 (2002) 824–833.
[27] M. Kleinschmidt, C.M. Marian, Chem. Phys. 311 (2005) 71–79.
[28] B.A. Hess, C.M. Marian, U. Wahlgren, O. Gropen, Chem. Phys. Lett. 251 (1996) 365–371.
[29] B. Schimmelpfennig, Stockholms University, 1996.
[30] J. Tatchen, C.M. Marian, Chem. Phys. Lett. 313 (1999) 351–357.
[31] D. Danovich, C.M. Marian, T. Neuheuser, S.D. Peyerimhoff, S. Shaik, J. Phys. Chem. A 102 (1998) 5923–5936.
[32] A. Toniolo, M. Persico, J. Chem. Phys. 115 (2001) 1817–1827.
[33] A. Toniolo, M. Persico, J. Comput. Chem. 22 (2001) 968–975.
[34] B.R. Henry, W. Siebrand, vol. 1, John Wiley & Sons, London, 1973.
[35] J. Tatchen, N. Gilka, C.M. Marian, Phys. Chem. Chem. Phys. 9 (2007) 5209–5221.
[36] J. Tatchen, Distort, Universität Düsseldorf, 2005.
[37] A. Klamt, G. Schürmann, J. Chem. Soc., Perkin Trans. 2 (1993) 799–805.
[38] A. Schäfer, A. Klamt, D. Sattel, J. Lohrenz, F. Eckert, Phys. Chem. Chem. Phys. 2 (2000) 2187–2193.
[39] C. Reichardt, Solvents and Solvent Effects in Organic Chemistry, VCH, Weinheim, 1990.
[40] K. Tomić, J. Tatchen, C.M. Marian, J. Phys. Chem. A 109 (37) (2005) 8410–8418.
[41] S. Salzmann, M. Kleinschmidt, J. Tatchen, R. Weinkauf, C.M. Marian, Phys. Chem. Chem. Phys. 10 (2008) 380–392.
[42] M. Wang, C.J. Fritchie Jr., Acta Crystallogr. (1973) 2040–2045.
[43] J. Tatchen, C.M. Marian, Phys. Chem. Chem. Phys. 8 (2006) 2133–2144.
[44] J.K. Eweg, F. Müller, A. Visser, C. Veeger, D. Bebelaar, J. van Voorst, Photochem. Photobiol. 30 (1979) 463–471.
[45] E.C. Lim, J. Phys. Chem. 90 (1986) 6770–6777.
[46] A. Losi, E. Polverini, B. Quest, W. Gärtner, Biophys. J. 82 (2002) 2627–2634.
[47] S. Perun, J. Tatchen, C.M. Marian, ChemPhysChem 9 (2008) 282–292.